Synergistic metabolism intervention and immune activation for antitumor therapy by biomineralized lactate oxidase

Yuxuan Ge[1], Zixin Wang[1], Yujia Lu[1], Fan Rong[1], Bin Hao[1], Zhao Li[2], Junsheng Chen[1,], and Yin Wang[1,*]*

1 Engineering Research Center of Cell & Therapeutic Antibody, Shanghai Frontiers Science Center of Drug Target Identification and Delivery, National Key Laboratory of Innovative Immunotherapy, School of Pharmaceutical Sciences, Shanghai Jiao Tong University, Shanghai 200240, China

2 InnoPep, Inc., San Diego 92121, United States

KEYWORDS

biomineralization, lactate oxidase, hydrogen sulfide, metabolism intervention, immunotherapy

ABSTRACT

Depleting tumoral lactate is a promising strategy to enhance the immune response and thereby suppressing tumorigenesis. However, the direct use of lactate oxidase (LOx), the most

straightforward lactate-eliminating agent, faces several issues including low stability, no targeting capacity. To solve these problems, a "carrier-free" nanodrug LOx@manganese sulfide (LOx@MnS) was facilely prepared via biomineralization. This way, all the constituents integrated in the nanodrug, including LOx, Mn^{2+}, and hydrogen sulfide (H_2S), could be readily delivered into tumor cells and exert their effects. LOx combined with Mn^{2+} to convert lactate to cytotoxic reactive oxygen species (ROS) through the cascade reaction, meanwhile the crosstalk between H_2S and ROS induced metabolism suppression to further augment the therapeutic efficacy. Consequently, the multi-mode therapeutic modalities led to effective immune activation and tumor suppression, suggesting the great potential for tumor treatment. We believe this strategy opens a new avenue to construct functional materials from frangible biomolecules and expand their applications.

INTRODUCTION

Generated by hyperactive glycolysis, lactate, a signaling molecule in tumor microenvironment (TME), plays an important role in promoting tumor invasion, metastasis as well as immunosuppression.[1-3] Accumulated lactate has been proven to upregulate the secretion of vascular endothelial growth factor (VEGF), prevent the activation of T lymphocytes, and induce M2 polarization of macrophages.[4] Hence, the depletion of lactate seems to be a promising strategy for tumor therapy.[5-11] Among various approaches, the most effective and straightforward way is the elimination of lactate by exogenous lactate oxidase (LOx) directly. LOx is a bacteria-sourced oxidase with flavin mononucleotide (FMN) prosthetic groups, which uses oxygen as the electron transfer substrate, and generates cytotoxic hydrogen peroxide (H_2O_2) through catalysis.[12] In terms of these aforementioned, LOx could be an ideal dual-functional enzyme for tumor therapy.[13-15] However, the application of LOx faces several practical issues including low stability, no targeting

capacity. Therefore, appropriate carriers are required for stability protection and targeting delivery, meanwhile additional therapeutic adjuvants are generally needed to boost the effect of LOx in the hypoxic TME. These obstacles result in the complicated preparation of most LOx-based formulations, which may bring extra metabolism burden and safety risk.

To solve these problems, a concise but powerful strategy called biomineralization has been adopted in the past few years. Inspired from nature biomineralized materials (e.g., bones and teeth), therapeutic ingredients could be facilely loaded into mineralized nanoparticles via a simple co-precipitation process.[16-18] Thus, the resultant materials possess some unique merits: they are generally biocompatible and biodegradable; payloads could be released through the dissolution in acidic conditions; the bioactivity of payloads could be well-preserved.[19] Moreover, the mineral itself could also work as the supplemental therapeutic agent if proper metal ions are intergraded. As for LOx, it is especially suitable for combining with manganese sulfide (MnS), because γ-MnS has a moderate aqueous solubility ($K_{sp} = 3 \times 10^{-11}$ at 25 °C) and a high propensity to crystalize via the metathesis reaction under neutral or alkaline condition. These features allow MnS to combine with temperature-sensitive proteins to form hybrid nanoparticles. Therefore, the as-prepared nanoparticles could keep stable in neutral condition but decompose in acid environment and release therapeutic agents, Mn^{2+} and hydrogen sulfide (H_2S).[20-22] Mn^{2+} could catalyze H_2O_2 to form hydroxyl radical (•OH) via Fenton-like reaction (so-called chemodynamic therapy, CDT);[23-26] concurrently, H_2S could suppress many heme-assisted enzymes, such as catalase (CAT), through binding to their catalytic centers,[27-29] meanwhile the crosstalk between H_2S and H_2O_2 would even trigger the *S*-persulfidation and deactivate many aspiration-related proteins to induce hypometabolism.[30-32] Collectively, rational combination of LOx and MnS would form a simple but self-adaptable system with multi-mode therapeutic activities.

Herein, in the present study, LOx was co-precipitated with MnS to construct "carrier free" nanodrug LOx@MnS nanoparticles (NPs) for tumor theranostic through in situ biomineralization (Figure 1). LOx not only worked as the therapeutic reagent, but also functioned as the template of nanoparticles during the preparation. Meanwhile, MnS acted as the H_2S donor and the catalyst for the cascade reaction of ROS generation. Upon internalization by tumor cells, NPs would degrade in acidic lysosome to unleash LOx, Mn^{2+}, and H_2S. Intracellular H_2O_2 was then accumulated under the synergy of LOx and H_2S, and finally converted into •OH. Moreover, reduced lactate and increased H_2S level would inhibit the cellular metabolism and relieve the immunosuppression. Beside tumor suppression, NPs also served as a contrast reagent of magnetic resonance imaging (MRI) due to the intratumoral release of Mn^{2+}, which further expanded the NPs' performance. Overall, this is an elaborate nanodrug realizing multi-functions (combination of enzyme therapy, CDT, gas therapy, and MRI monitoring) through simple design, i.e., one-step preparation from two ingredients.

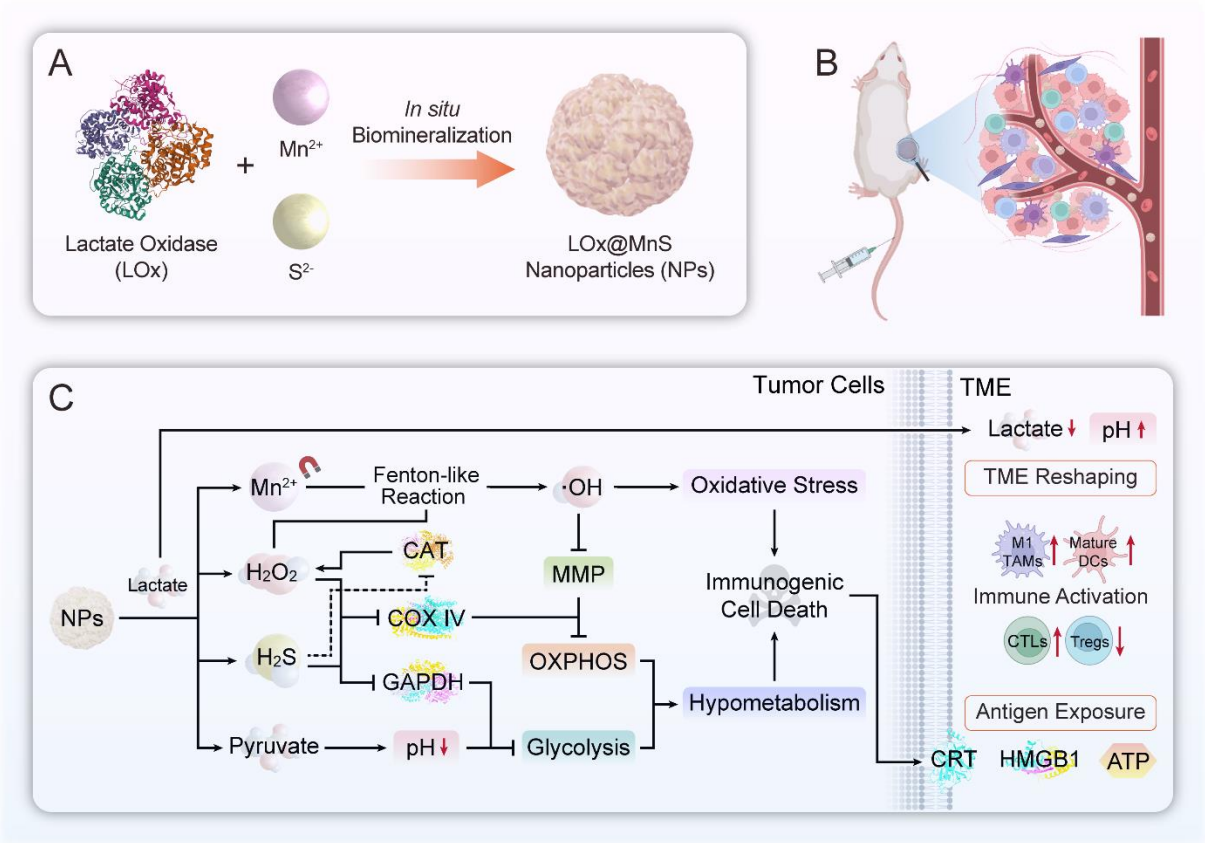

Figure 1. A schematic diagram of the preparation process (A), administration (B), and pharmacological mechanism (C) of LOx@MnS NPs.

RESULTS AND DISCUSSION

The preparation of LOx@MnS NPs followed a one-step biomineralization method. Since the formation of hybrid NPs relied on the *in situ* crystallization of minerals on the surface of proteins, we firstly checked the crystallization capability of chosen minerals at normal temperature and pressure. Besides MnS mentioned before, another typical mineral H_2S donor, zinc sulfide (ZnS), was also prepared using the same method to verify the feasibility of biomineralization. Surprisingly, although ZnS had the similar pH-responsive degradation property with MnS, the

metathesis reaction between Zn^{2+} and HS^- under neutral condition could only afford fragmented and subcrystalline ZnS aggregates regardless of presence of the template (Figure S1A and Figure S1B). The possible reason was that ZnS carried superfluous water during the precipitate process at low temperature. The necessary process to get uniform ZnS particles was the re-crystallization of ZnS under high pressure and temperature (e.g., the hydrothermal method used in most studies for ZnS)[33-35] (Figure S1C). Nevertheless, MnS exhibited much better crystallization capability, i.e., the metathesis reaction at low temperature could lead to the formation of compact small crystals even without any template or stabilizer (Figure S1D). Notably, the morphology of MnS could be further optimized when suitable templates were applied (e.g., LOx used in the present study) (Figure S1E), suggesting the unique advantages of MnS in the application of biomineralization. MnS could also be prepared via the hydrothermal method,[36] but the co-precipitate way was much simpler and more easily to operate. Importantly, it realized the direct encapsulation of fragile proteins during the preparation of mineralized nanoparticles, exhibiting great potential as a nanoplatform for protein-based nanodrugs. As shown in Figure 2A, the as-prepared LOx@MnS NPs were spherical-like with a coarse surface, and main elements representing LOx and MnS (C, N, O, S, and Mn) were uniformly distributed inside the NPs (Figure 2B), suggesting that NPs were formed via the aggregation of LOx-MnS nanocomposites. It should be noted that the crystallization rate of MnS was positively related to the pH value and bigger particle size was generated at higher pH (Figure S2). The co-precipitation at pH 7.4 endowed the best morphology (average hydrodynamic size = 191.7 nm, polydispersity index (PDI) = 0.061) (Figure 2C) and good colloidal stability (zeta-potential = -25.1 mV) (Figure S3) of NPs, thus these reaction parameters were used for the large batch synthesis of NPs. X-ray diffraction (XRD) pattern of NPs confirmed that the crystal form of MnS was γ-phase (Figure 2D). In addition, the spectra of ultraviolet-visible

spectroscopy (UV-vis) and Fourier transform-infrared spectroscopy (FT-IR) containing characteristic absorption bands of LOx further verified the encapsulation of LOx in NPs (Figure S4 and Figure 2E). The secondary structure of encapsulated LOx was also proved to kept stable after mineralization according to circular dichroism (CD) spectra (Figure 2F). Thus, we could preliminarily verify the successful preparation of NPs.

Subsequently, the activities of both ingredients in NPs were tested. As for pH-responsive H_2S releasing behavior, NPs (50 μg / mL) were incubated in 25 mM acetate buffer at different pHs (7.4 or 5.5). NPs showed little degradation at pH 7.4 but sustainably release H_2S in 1 h at pH 5.5, and the maximum concentration of H_2S reached to ~60 μM (Figure 2G). The enzymatic activity of loaded LOx was then checked via detecting generation of pyruvate and H_2O_2. Surprisingly, the catalytic activity of loaded LOx nearly emerged no attenuation compared with free LOx. No significant difference was shown in the generation kinetics of pyruvate (Figure 2H and Figure S5) and H_2O_2 (Figure 2I, Figure 2J and Figure S6). Given that both groups were well fitted to Michaelis-Menten kinetics and Lineweaver-Burk plot of enzyme catalysis, it indicated that MnS mineralization could effectively maintain the enzyme activity of LOx. As the last step of cascade reaction to generate cytotoxic ROS, Mn^{2+}-mediated Fenton-like reaction was then investigated by the methylene blue (MB) decolorization. Coexistence of NPs and H_2O_2 could rapidly generate •OH and fade the color of MB, meanwhile similar results were also obtained when H_2O_2 was replaced with lactate (Figure 2K and Figure S7), demonstrating the feasibility of NPs as a cascade reagent. Lastly, the MRI capacity of NPs was verified (Figure 2L). The T_1-weighted signal displayed well positive correlation with the concentration of released Mn^{2+}, and the longitudinal relaxation rate (r_1) was calculated to be 12.54 mM^{-1} s^{-1}. Collectively, the theranostic potential of NPs for cancer treatment was carefully validated *in vitro*.

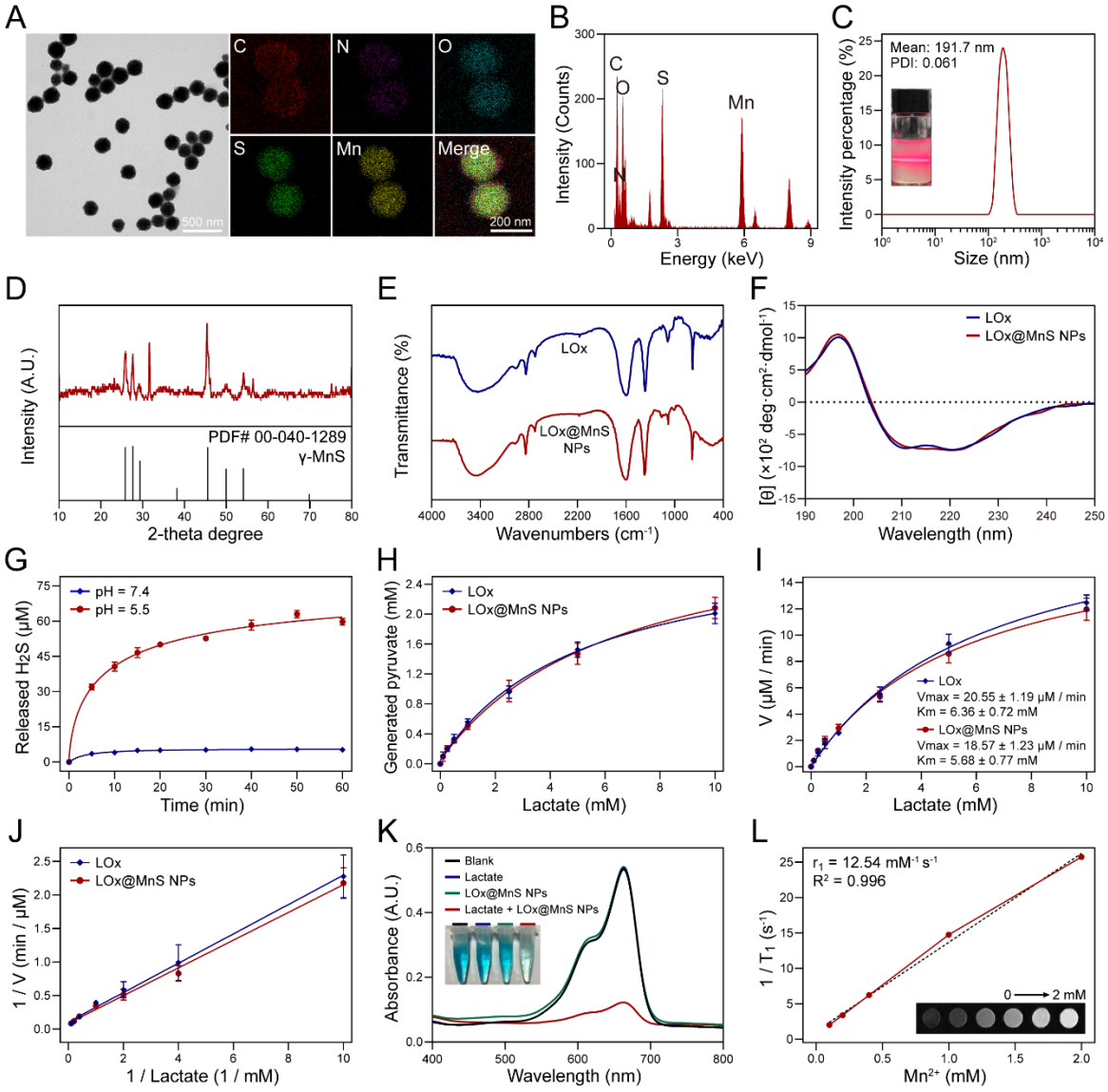

Figure 2. Characterization of LOx@MnS NPs. (A) Representative transmission electron microscope (TEM) image and elemental mappings of NPs. (B) Energy dispersive spectroscopy (EDS) of NPs. (C) Dynamic light scattering (DLS) curve and Tyndall effect of NPs in water. (D) XRD pattern of NPs, compared with standard γ-MnS. (E) FT-IR spectra of NPs and free LOx. (F) CD spectra of NPs and free LOx. (G) H_2S release curves of NPs in 25 mM acetate buffer (pH 7.4 or 5.5). (H) Pyruvate generation from different concentrations of lactate in 3 h. (I) Michaelis-

Menten kinetics and (J) Lineweaver-Burk plots of NPs and free LOx based on H_2O_2 generation from different concentrations of lactate in 3 h. V_{max}: maximum initial velocity, K_m: Menten constant. (K) UV-vis spectra and image of MB degradation incubated with 10 mM of lactate and / or NPs for 2 h. NPs = 50 μg / mL, LOx = 15 μg / mL for F-K. (L) *In vitro* MRI and T_1 relaxation rate ($1 / T_1$) of NPs at pH 5.5.

With NPs in hands, we then investigated the catalytic performance of NPs and its effect on anti-tumor activity (Figure 3A). The cytotoxicity of NPs was initially explored on mouse breast cancer 4T1 tumor cells. After being internalized into cells (Figure 3B), NPs exhibited remarkable and selective cytotoxicity (Figure 3C), which was due to higher intracellular lactate level of 4T1 cells compared with normal human umbilical vein endothelial cells (HUVEC) (Figure 3D). Meanwhile, the cytotoxicity and pro-apoptosis effect of NPs were significantly higher than either bare MnS or LOx, further verifying the importance of rational combination of both components. It would ensure the cascade reaction of ROS generation (Figure 3E-Figure 3G). As mentioned above, the internalization of NPs into cells would lead to their degradation and H_2S release. After co-incubation with cells for 4 h, both MnS and NPs demonstrated strong intracellular green fluorescence (by H_2S probe) (Figure 3H), which were able to reduce CAT activity (Figure 3I). At last, the product from the synergized interaction from LOx and H_2S, reactive oxygen species (ROS, including H_2O_2 and •OH), were detected using 2', 7'-dichlorodihydrofluorescein diacetate (DCFH-DA) probe (Figure 3J). It could be seen that although MnS itself did not significantly induce the generation of ROS, it served as a good CDT sensitizer and remarkably amplified the ROS generation by LOx. Obviously, the ROS generation capacity of NPs contributed to the excellent anti-proliferation activity *in vitro* and anti-tumor ability *in vivo* (discussed below).

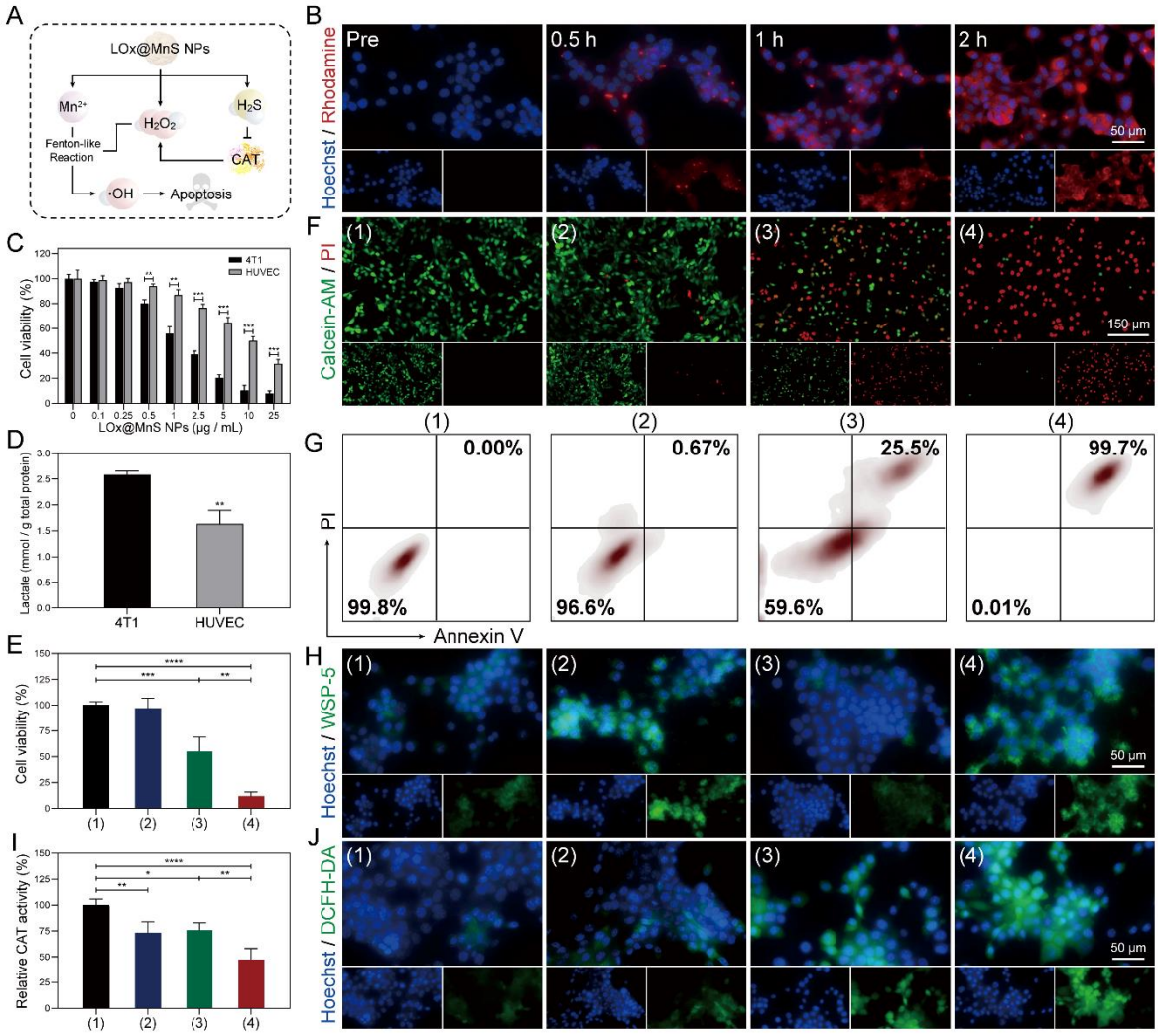

Figure 3. *In vitro* antitumor capability of LOx@MnS NPs. (A) Illustration of ROS generation by NPs. (B) Cellular uptake of NPs incubated with different times (NPs were labeled with Rhodamine B). (C) Cell viability of 4T1 and HUVEC cells treated with NPs at different concentrations for 24 h. (D) Intracellular lactate levels of native 4T1 and HUVEC cells. (E) Cell viability of 4T1 cells with different treatments for 24 h. (F) Calcein-AM / propidium iodide (PI) fluorescent staining of 4T1 cells with different treatments for 24 h. (G) Annexin V-fluorescein isothiocyanate (FITC) / PI flow cytometry analysis of 4T1 cells with different treatments for 24 h. (H) Washington State Probe-5 (WSP-5) fluorescent staining of 4T1 cells with different treatments for 4 h. (I) Relative

CAT activity of 4T1 cells with different treatments for 4 h. (J) DCFH-DA fluorescent staining of 4T1 cells with different treatments for 4 h. (1) Control, (2) MnS (60 μM), (3) LOx (3 μg / mL), (4) LOx@MnS NPs (10 μg / mL). * $P < 0.05$, ** $P < 0.01$, *** $P < 0.001$, **** $P < 0.0001$, analyzed by one-way analysis of variance (ANOVA).

The mechanism of inhibiting tumor cell proliferation was then further elucidated through a series of biochemical analysis (Figure 4A). Considering that lactate is the end product of glycolysis, and H_2S has been reported to impact some metabolism-related enzymes, the influences of NPs on glycolysis were then analyzed. Intracellular detection lactate assay affirmed LOx could deplete the lactate (Figure 4B). Meanwhile, the key enzyme of glycolysis, glyceraldehyde-3-phosphate dehydrogenase (GAPDH), was found to be deactivated by NPs treatment (Figure 4C). Compared with native 4T1 cells, NPs treated cells exhibited over 80 % inhibition rate on GAPDH activity, yet which of MnS and LOx treated ones were only ~15 % and ~45 %. This may be attributed to the *S*-persulfidation of GAPDH driven by the crosstalk between H_2S and H_2O_2.[37] Besides, the depletion of lactate and suppression of glycolysis would lead to the accumulation of intracellular glucose and pyruvate. Glucose detection confirmed this hypothesis that NPs treated cells showed a ~1.7-fold increase in glucose level compared with native cells, implying glucose consumption was attenuated (Figure 4D). Concurrently, pyruvate accumulation was indirectly verified using the pH probe 2', 7'-bis(2-carboxyethyl)-5(6)-carboxyfluorescein acetoxymethyl ester (BCECF-AM). Because of the stronger acidity of pyruvate (pKa = 2.50) compared with lactate (pKa = 3.86), the extensive conversion from lactate to pyruvate would decline the intracellular pH, which quenched the fluorescence of BCECF-AM (representing the pH decrease) in cells treated with LOx or NPs (Figure 4E). Additionally, the depletion of lactate also inhibited the lactate efflux pathway, which in turn resulted in the increment of medium pH (Figure S8).

Besides glycolysis suppression, the effect of NPs on damaging respiratory chain in mitochondria was also studied. Nicotinamide adenine dinucleotide (NAD) was the key coenzyme for the electron transport in oxidative phosphorylation (OXPHOS), and the ratio of oxidized NAD (NAD^+) to reduced NAD (NADH) reflected the status of respiratory chain. Approximately 1.5 or 2-fold increase of [NAD^+] : [NADH] ratio was found for cells treated with LOx or NPs respectively, manifesting that NADH-generating reactions in these cells were disturbed (Figure 4F and Figure S9). Due to NADH exhaustion, generation of adenosine triphosphate (ATP) was also constrained by ~50 % for LOx treated group and ~64 % for NPs treated one (Figure 4G). Clearly, interruption of these biochemical reactions somehow confirmed the mitochondrial dysfunction. Fluorescent imaging by JC-1 probe was then proceeded to observe the change on mitochondrial membrane potential (MMP). The red fluorescence (representing JC-1 aggregates in high MMP) was substantially shifted to the green fluorescence (representing JC-1 monomers in low MMP) when cells were treated with LOx or NPs, with NPs inducing a more thorough change (Figure 4H). According to numerous existing studies and the result of ROS detection (Figure 3J), it was easy to draw a conclusion that ROS caused oxidative stress which further induced the mitochondrial damage and thereby blocking the respiratory chain. However, NPs could disturb the respiratory chain through another pathway. It has been reported that H_2S could inhibit many heme-assisted enzymes, including the key enzyme complex in respiratory chain, complex IV (COX IV).[38] Hence, we further monitored whether the released H_2S from NPs could suppress COX IV and enhance the blockade of the respiratory chain. As demonstrated by the COX IV immunofluorescent imaging, the COX IV expression was significantly decreased after NPs treatment (Figure 4I). Collectively, these results confirmed that NPs could synchronously suppress both glycolysis and OXPHOS via

lactate depletion, ROS generation as well as H_2S release, and finally transforming tumor cells into a hypometabolic phenotype, which would be beneficial for the suppression of cancer cell growth.

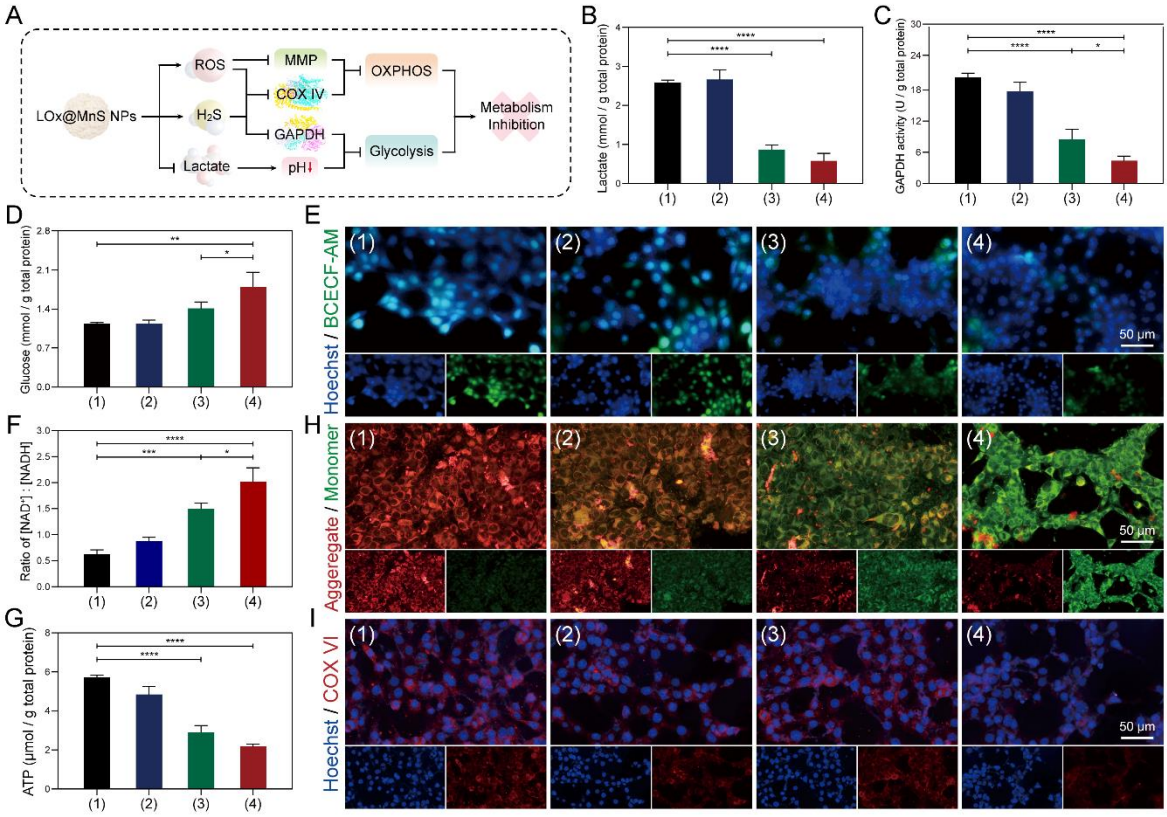

Figure 4. *In vitro* metabolism suppression effect of LOx@MnS NPs. (A) Schematic illustration of the metabolism suppressing pathways. (B) Intracellular lactate levels of 4T1 cells with different treatments for 12 h. (C) GAPDH activities of 4T1 cells with different treatments for 12 h. (D) Intracellular glucose levels of 4T1 cells with different treatments for 12 h. (E) BCECF-AM fluorescent imaging of 4T1 cells with different treatments for 12 h. (F) Intracellular $[NAD^+]$: [NADH] ratios in 4T1 cells with different treatments for 12 h. (G) Intracellular ATP contents of 4T1 cells with different treatments for 12 h. (H) JC-1 fluorescent imaging of 4T1 cells with different treatments for 12 h. (I) COX IV immunofluorescent imaging of 4T1 cells with different

treatments for 12 h. (1) Control, (2) MnS (60 μM), (3) LOx (3 μg / mL), (4) LOx@MnS NPs (10 μg / mL). * $P < 0.05$, ** $P < 0.01$, *** $P < 0.001$, **** $P < 0.0001$, analyzed by one-way ANOVA.

As mentioned above, accumulated lactate in TME would result in immunosuppression and induce polarization of macrophages to M2 subtypes, whereas NPs could reverse the dilemma by decreasing the lactate level as well as inducing immunogenic cell death (ICD) of tumor cells (Figure 5A). As demonstrated in Figure 5B, LOx alone was capable of reducing the secreted lactate of 4T1 cells from 4 mM to less than 0.5 mM, which eliminated one of major inducing factors of immunosuppression. Furthermore, NPs treatment caused the excessive ROS accumulation and metabolism suppression, which would promote ICD.[39-44] Besides, ATP acted as a "find me" signal for antigen-presenting cells (APCs), and ATP was not generally released to the extracellular environment for native tumor cells. Nevertheless, LOx or NPs treatment could effectively break the homeostasis and increase the release of ATP to 0.6 mM or 1.3 mM, respectively (Figure 5C). Translocation of Calreticulin (CRT) from endoplasmic reticulum to cell surface was another typical damage-associated molecular pattern (DAMP) to trigger the antigen uptake and phagocytosis. Immunofluorescent staining of surface CRT indicated that only NPs treatment successfully stimulated the translocation (Figure 5D), further validating the antigen exposure effect endowed by NPs. The third typical factor was the high mobility group box 1 (HMGB1), a nuclear cytokine with immune activating capacity. Although HMGB1 kept binding with nuclear DNA in native 4T1 cells, LOx or NPs treatment would induce its leakage to cytoplasm and even extracellular environment, thereby causing the diffusion and quenching of the immunofluorescent signals of HMGB1 (Figure 5E). Strikingly, cells treated with NPs showed the most evident antigen exposure, encouraging us to further investigate whether treatment of NPs could practically generate the immune response.

The *in vitro* assessment was then proceeded through co-incubation of 4T1 tumor cells with different treatments and mouse macrophage RAW264.7 cells, and the macrophage polarization was tested via monitoring cluster of differentiation 86 (CD86, M1 marker) as well as CD206 (M2 marker) through flow cytometry. As demonstrated in Figure S10 and Figure 5F, high concentration of tumor-sourced lactate induced a higher ratio of M2 ($CD86^{low}$ / $CD206^{high}$) macrophages (from 17.9 % to 38.7 %), while pre-treatment of MnS on 4T1 cells could reduce the ratio to 25.9 %. Notably, lactate depleting and ICD inducing capacity endowed by LOx and NPs further reduced the ratio of M2 macrophages to 5.86 % and 3.78 %, respectively (Figure S11A). Correspondingly, the ratio of anti-tumoral M1 ($CD86^{high}$ / $CD206^{low}$) macrophage was elevated from 5.82 % (control) and 8.23 % (MnS treated) to 25.1 % (LOx treated) and 30.3 % (NPs treated) (Figure S11B). The level of several pro-inflammatory molecules secreted by M1 macrophages, including nitric oxide (NO) (Figure 5G), tumor necrosis factor-α (TNF-α) (Figure 5H), and interleukin-6 (IL-6) (Figure 5I), kept consistent with the macrophage polarization test, with LOx pre-treatment on 4T1 cells stimulating their secretion, meanwhile NPs leading to a significantly higher up-regulation. Moreover, the remarkable decline of the typical anti-inflammatory cytokine IL-10 (mainly produced by M2 macrophage) observed in MnS, LOx, and NPs treated groups further strengthened the trend (Figure 5J). Relying on these results, we could deduce that NPs were able to reprogram the TME and reinforce the immune response.

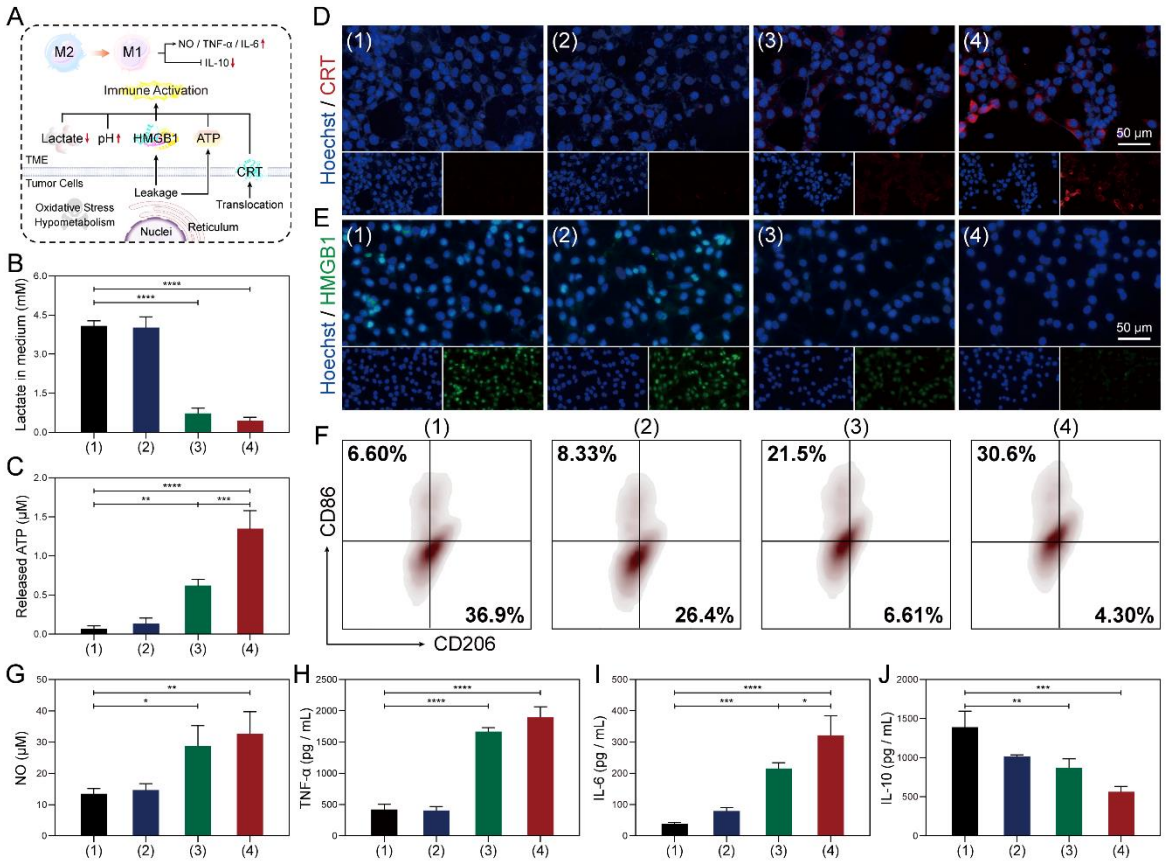

Figure 5. *In vitro* immune activating effects of LOx@MnS NPs. (A) Schematic illustration for the mechanism of immune modulation by NPs. (B) Lactate levels in medium of 4T1 cells with different treatments for 12 h. (C) Leaked ATP levels in medium of 4T1 cells with different treatments for 12 h. (D) CRT immunofluorescent imaging of 4T1 cells with different treatments for 12 h (without permeabilization treatment). (E) HMGB1 immunofluorescent imaging of 4T1 cells with different treatments for 12 h. (F) Flow cytometry analysis on CD86 / CD206 of RAW264.7 cells after co-incubation with 4T1 cells for 24 h. (G) NO, (H) TNF-α, (I) IL-6, and (J) IL-10 levels in medium of RAW264.7 cells after co-incubation with 4T1 cells for 24 h. (1) Control, (2) MnS (60 μM), (3) LOx (3 μg / mL), (4) LOx@MnS NPs (10 μg / mL). * $P < 0.05$, ** $P < 0.01$, *** $P < 0.001$, **** $P < 0.0001$, analyzed by one-way ANOVA.

Encouraged by the excellent outcomes of cell killing, metabolism inhibition, and immune activation *in vitro*, the therapeutic effects of NPs were then analyzed on 4T1 tumor-bearing mice (Figure 6A). First, the accumulation of NPs in the tumor site was evaluated utilizing their MRI contrast feature. The strengthened MRI signal could be clearly observed in the tumor site in 6 h post-intravenous injection (up to 1.97-fold enhancement at 6 h), then the signal gradually weakened with the prolonged time but still kept strongly contrasting to the pre-injection (1.68-fold at 24 h) (Figure S12). These results proved that NPs could effectively accumulate in the tumor site for a long time. As expected, treatment with NPs achieved the most remarkable tumor inhibition rate (72.0 %) after 14 d. In contrast, treating with MnS or LOx alone could only inhibit the tumor growth by 37.0 % or 30.9 %, respectively. The possible reason for this phenomenon might be the insufficiently intracellular H_2O_2 content (Figure 6B, Figure 6C, and Figure S13). The tumor weights on day 14 showed the consistent results, with NPs treatment reducing the average tumor weight from 1.68 g to 0.28 g. However, the weights of MnS or LOx treated group were 1.02 g or 0.88 g (Figure 6D). Besides, no significant body weight loss was observed in all 4 groups during the treatment (Figure 6E). Combined with the ultra-low hemolysis rate (Figure S14) and pathological examinations (including H&E staining of main organs, routine blood tests, and blood biochemical indexes) (Figure S15 - Figure S17), we could conclude that NPs had excellent biocompatibility. Pathological analysis of tumor slices further verified the superior anti-tumor effect of NPs. The hematoxylin & eosin (H&E) staining and terminal deoxynucleotidyl transferase-mediated nick end labeling (TUNEL) exhibited that tumors treated with NPs underwent severe cell apoptosis and necrosis, accompanying with the down-regulation of proliferation-related antigen Ki67 (Figure 6F).

Finally, the immune activation status on the tumor-bearing mice was synchronously checked. Parts of mice were sampled on day 7 to investigate the in vivo lactate depletion capability of NPs. It was found that only NPs treatment could effectively lower the intratumoral lactate content for 64.8 % (Figure 6G), whereas LOx alone severely reduced serum lactate but did not show apparent effect in tumor site (Figure S18). Obviously, the targeted lactate elimination would help to reshape the immunosuppressive TME. A typical indicator for the anti-tumor immune response, interferon-γ (IFN-γ), was up-regulated by 1.73-fold in the serum of mice with NPs treatment, suggesting that the immune response was activated (Figure 6H). The immune cells infiltrated in tumors were then investigated via the flow cytometry. NPs treatment could up-regulate the population of $CD8^+$ cytotoxic T lymphocytes (CTLs) by 2.22-fold (Figure 6I and Figure S19A). In the meantime, the percentage of forkhead box protein P3 $(FoxP3)^+$ regulatory T lymphocytes (T_{reg} cells) in $CD4^+$ helper T lymphocytes (T_h cells) was greatly decreased by 57.9 % (Figure 6J and Figure S19B), and the population of infiltrated M1 macrophages raised from 16.7 % to 21.6 % (M1 / M2 ratio increased by 1.36-fold) (Figure 6K and Figure S19C), indicating the successful reverse of immune inhibition in TME. Beside the terminal tumor-killing immune cells, both lactate depletion and ICD induction by NPs also triggered the activation of immune response and immune memory. The percentage of $CD80^+$ / $CD86^+$ maturated dendritic cells (DCs) was lifted from 14.0 % to 21.9 % after NPs treatment (Figure 6L and Figure S19D), implying the effective antigen presentation enhancement endued by NPs. Increased population of $CD44^+$ / $CD62L^-$ effector memory T cells (T_{em} cells) was also found in spleens of mice treated with NPs, which represented that their immune systems had successfully gained the anti-tumor immune memory (Figure 6M and Figure S19E).

To inspect whether the immune memory induced by NPs treatment could prevent tumor metastasis, parts of mice were intravenously injected with 4T1 cells after 14 d treatment to build the lung

metastasis model. After growth for 14 d, the metastasized tumor cells colonized the full lungs and resulted in the “fried” appearance of the surface. Mice with MnS or LOx treatment showed fewer metastasis nodules on the surface of their lungs, yet the H&E staining of lung slices declared that these lungs were still severely damaged by infiltrated tumor cells (Figure 6N). Only NPs treatment protected these mice from tumor metastasis that almost no metastasis nodule could be observed either on the surface or inside the lobes (Figure 6O and Figure 6P). Hence, the anti-tumor immunity activated by NPs could be maintained and prevent mice from tumor metastasis.

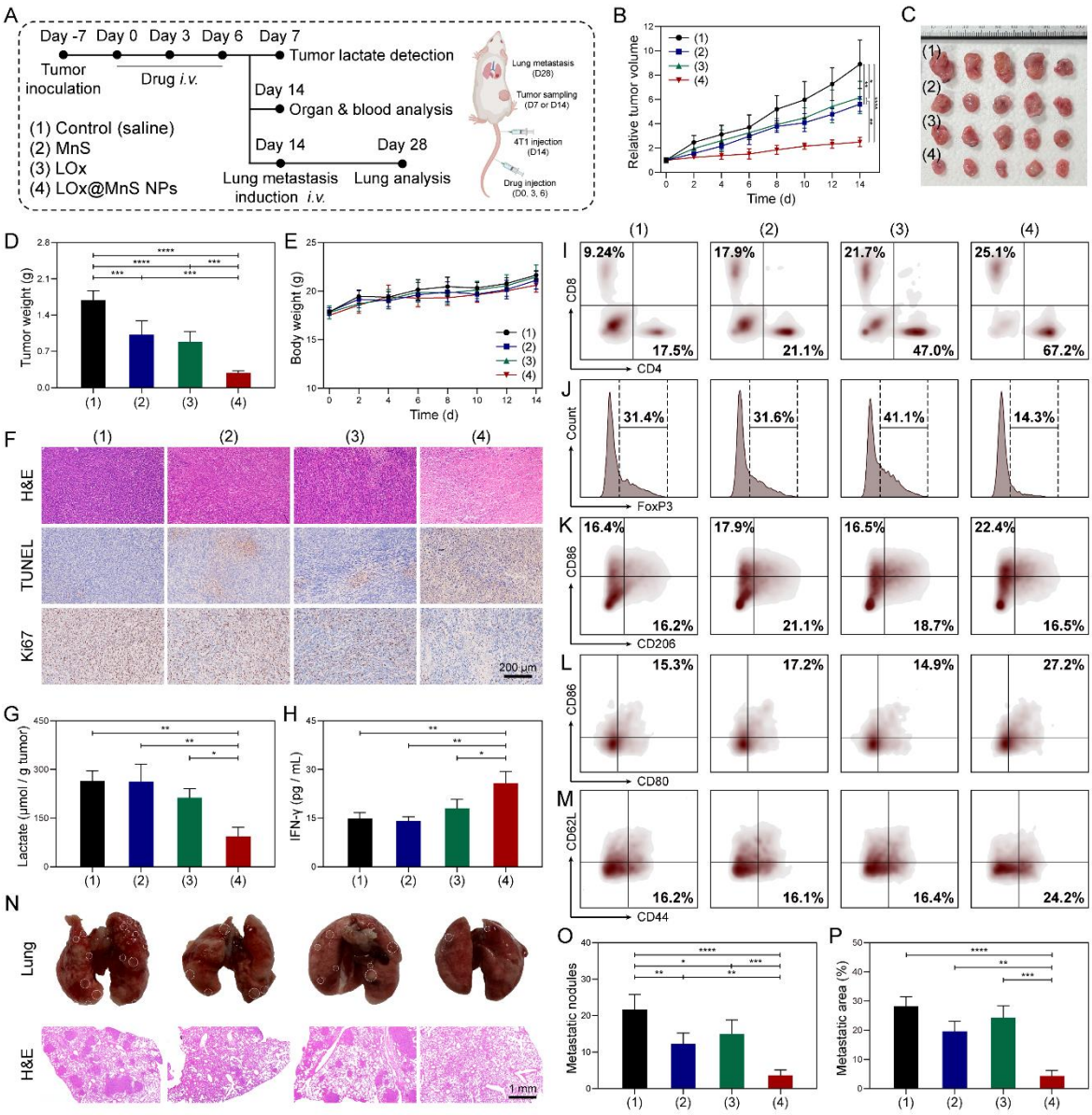

Figure 6. *In vivo* anti-tumor and immune activation capabilities of LOx@MnS NPs. (A) Treatment protocol for the *in vivo* studies. (B) Tumor volume variations within 14 d. (C) Representative photographs of tumors on 14 d post-treatment. (D) Tumor weights on 14 d post-treatment. (E) Body weights of mice during the 14 d. (F) Histopathological staining of tumor slices (H&E, TUNEL, and Ki67). (G) Lactate contents in tumor tissues at day 7. (H) Serum IFN-γ levels of mice at day 7. (I) Population of CTLs / T_h cells infiltrated into the tumor sites. (J) Population of T_{reg}

cells. (K) Population of M1 / M2 macrophages in the tumor site. (L) Population of mature DCs in spleen. (M) Population of T_{em} cells in spleen. (N) Representative photographs and H&E staining of lungs with different treatments. (O) Number of metastatic nodules in lungs with different treatments. (P) Replacement area (%) of metastatic nodules in lungs with different treatments. * $P < 0.05$, ** $P < 0.01$, *** $P < 0.001$, **** $P < 0.0001$, analyzed by one-way ANOVA.

CONCLUSION

In the present study, we reported a facile "carrier free" nanodrug, LOx@MnS NPs, for multi-mode tumor treatment. The design and preparation of NPs utilized the easy-to-crystallize and pH-responsive degradation characters of MnS to realize the in situ mineralization with LOx. Thus, the as-prepared NPs could simply encapsulate LOx without suppressing its activity, keep stable in the neutral condition and directly release LOx, Mn^{2+}, and H_2S in the TME via acid-responsive degradation. These released ingredients could simultaneously induce strong oxidative stress through the lactate - H_2O_2 - •OH cascade reaction, and further achieve metabolism inhibition by deactivation of multiple enzymes contributed by the crosstalk between H_2S and H_2O_2. The synergistic multi-pathway finally led to the effective tumor killing as well as the reverse of immunosuppressive TME. These features endowed NPs with excellent anti-tumor and immune activation capabilities, demonstrating the considerable therapeutic potential. Moreover, along with the deeping of researches on therapeutic proteins and other biomacromolecules, the pattern of constructing mineral-based nanodrugs by biomineralization could be further expanded to cope with various diseases.

ASSOCIATED CONTENT

Supporting Information

Supporting Information file is available free of charge.

Including materials, preparation of LOx@MnS NPs, characterization, enzymatic activity assays, *in vitro* anti-tumor assays, *in vitro* metabolism assays, *in vitro* immunomodulatory assays, tumor-bearing mice models, and corresponding supplemental figures S1 - S19 (PDF).

AUTHOR INFORMATION

Corresponding Authors

Yin Wang* - Engineering Research Center of Cell & Therapeutic Antibody, Shanghai Frontiers Science Center of Drug Target Identification and Delivery, National Key Laboratory of Innovative Immunotherapy, School of Pharmaceutical Sciences, Shanghai Jiao Tong University, Shanghai 200240, P.R. China. E-mail: yinwang@sjtu.edu.cn.

Junsheng Chen* - Engineering Research Center of Cell & Therapeutic Antibody, School of Pharmaceutical Sciences, Shanghai Jiao Tong University, Shanghai 200240, P.R. China. E-mail: js.chan@sjtu.edu.cn.

Author Contributions

The manuscript was written through contributions of all authors. All authors have given approval to the manuscript.

Notes

The authors declare no conflict of interests.

ACKNOWLEDGMENT

Financial support from the National Natural Science Foundation of China (22375128, 22105126), the Natural Science Foundation of Shanghai (22ZR1433500), the Open Project Program of Engineering Research Center of Cell & Therapeutic Antibody, Ministry of Education, Shanghai Jiao Tong University (22 × 010201609004), and startup funding from Shanghai Jiao Tong University is acknowledged. Some image icons used in figures were gained from BioRender.com and RCSB Protein Data Bank (RCSB PDB). We also thank Ms. Wei Li and Dr. Dan Lyu for their helpful discussion and assists.

REFERENCES

(1) Wang, Z. H.; Peng, W. B.; Zhang, P.; Yang, X. P.; Zhou, Q., Lactate in the tumour microenvironment: from immune modulation to therapy. *EBioMedicine.* **2021,** *73*, 103627.

(2) Zhao, J.; Tian, Z.; Zhao, S.; Feng, D.; Guo, Z.; Wen, L.; Zhu, Y.; Xu, F.; Zhu, J.; Ma, S.; Hu, J.; Jiang, T.; Qu, Y.; Chen, D.; Liu, L., Insights into the effect of catalytic intratumoral lactate depletion on metabolic reprogramming and immune activation for antitumoral activity. *Adv Sci (Weinh).* **2023,** *10* (4), e2204808.

(3) Zhao, S.; Li, H.; Liu, R.; Tao, N.; Deng, L.; Xu, Q.; Hou, J.; Sheng, J.; Zheng, J.; Wang, L.; Chen, W.; Guo, S.; Liu, Y. N., Nitrogen-centered lactate oxidase nanozyme for tumor lactate modulation and microenvironment remodeling. *J Am Chem Soc.* **2023,** *145* (18), 10322-10332.

(4) Morland, C.; Andersson, K. A.; Haugen, O. P.; Hadzic, A.; Kleppa, L.; Gille, A.; Rinholm, J. E.; Palibrk, V.; Diget, E. H.; Kennedy, L. H.; Stolen, T.; Hennestad, E.; Moldestad, O.; Cai,

Y.; Puchades, M.; Offermanns, S.; Vervaeke, K.; Bjoras, M.; Wisloff, U.; Storm-Mathisen, J.; Bergersen, L. H., Exercise induces cerebral VEGF and angiogenesis via the lactate receptor HCAR1. *Nat Commun.* **2017,** *8*, 15557.

(5) Lu, G.; Wang, X.; Li, F.; Wang, S.; Zhao, J.; Wang, J.; Liu, J.; Lyu, C.; Ye, P.; Tan, H.; Li, W.; Ma, G.; Wei, W., Engineered biomimetic nanoparticles achieve targeted delivery and efficient metabolism-based synergistic therapy against glioblastoma. *Nat Commun.* **2022,** *13* (1), 4214.

(6) Li, K.; Lin, C.; He, Y.; Lu, L.; Xu, K.; Tao, B.; Xia, Z.; Zeng, R.; Mao, Y.; Luo, Z.; Cai, K., Engineering of cascade-responsive nanoplatform to inhibit lactate efflux for enhanced tumor chemo-immunotherapy. *ACS Nano.* **2020,** *14* (10), 14164-14180.

(7) Chen, Z. X.; Liu, M. D.; Zhang, M. K.; Wang, S. B.; Xu, L.; Li, C. X.; Gao, F.; Xie, B. R.; Zhong, Z. L.; Zhang, X. Z., Interfering with lactate-fueled respiration for enhanced photodynamic tumor therapy by a porphyrinic MOF nanoplatform. *Adv Funct Mater.* **2018,** *28* (36), e1803498.

(8) Gao, F.; Tang, Y.; Liu, W. L.; Zou, M. Z.; Huang, C.; Liu, C. J.; Zhang, X. Z., Intra/extracellular lactic acid exhaustion for synergistic metabolic therapy and immunotherapy of tumors. *Adv Mater.* **2019,** *31* (51), e1904639.

(9) Lu, Y.; Wang, Y.; Liu, W.; Ma, H.; Yang, B.; Shao, K.; Long, S.; Sun, W.; Du, J.; Fan, J.; Liu, B.; Wang, L.; Peng, X., Photothermal "nano-dot" reactivate "immune-hot" for tumor treatment via reprogramming cancer cells metabolism. *Biomaterials.* **2023,** *296*, 122089.

(10) Wang, J. W.; Chen, Q. W.; Luo, G. F.; Han, Z. Y.; Song, W. F.; Yang, J.; Chen, W. H.; Zhang, X. Z., A self-driven bioreactor based on bacterium-metal-organic framework biohybrids for boosting chemotherapy via cyclic lactate catabolism. *ACS Nano.* **2021,** *15* (11), 17870-17884.

(11) Tseng, S. J.; Kempson, I. M.; Huang, K. Y.; Li, H. J.; Fa, Y. C.; Ho, Y. C.; Liao, Z. X.; Yang, P. C., Targeting tumor microenvironment by bioreduction-activated nanoparticles for light-triggered virotherapy. *ACS Nano.* **2018,** *12* (10), 9894-9902.

(12) Hiraka, K.; Yoshida, H.; Tsugawa, W.; Asano, R.; La Belle, J. T.; Ikebukuro, K.; Sode, K., Structure of lactate oxidase from Enterococcus hirae revealed new aspects of active site loop function: product-inhibition mechanism and oxygen gatekeeper. *Protein Sci.* **2022,** *31* (10), e4434.

(13) Cao, Z.; Xu, D.; Harding, J.; Chen, W.; Liu, X.; Wang, Z.; Wang, L.; Qi, T.; Chen, S.; Guo, X.; Chen, I. S. Y.; Guo, J.; Lu, Y.; Wen, J., Lactate oxidase nanocapsules boost T cell immunity and efficacy of cancer immunotherapy. *Sci Transl Med.* **2023,** *15* (717), eadd2712.

(14) Choi, H.; Yeo, M.; Kang, Y.; Kim, H. J.; Park, S. G.; Jang, E.; Park, S. H.; Kim, E.; Kang, S., Lactate oxidase/catalase-displaying nanoparticles efficiently consume lactate in the tumor microenvironment to effectively suppress tumor growth. *J Nanobiotechnol.* **2023,** *21* (1), 5.

(15) Jiang, S.; Chen, X.; Lin, J.; Huang, P., Lactate-oxidase-instructed cancer diagnosis and therapy. *Adv Mater.* **2023,** *35* (19), e2207951.

(16) Li, Q.; Dong, Z.; Cao, Z.; Lei, H.; Wang, C.; Hao, Y.; Feng, L.; Liu, Z., A general biomineralization strategy to synthesize autologous cancer vaccines with cGAS-STING activating capacity for postsurgical immunotherapy. *ACS Nano.* **2023,** *17* (11), 10496-10510.

(17) Chen, Q.; Wang, C.; Zhang, X.; Chen, G.; Hu, Q.; Li, H.; Wang, J.; Wen, D.; Zhang, Y.; Lu, Y.; Yang, G.; Jiang, C.; Wang, J.; Dotti, G.; Gu, Z., In situ sprayed bioresponsive immunotherapeutic gel for post-surgical cancer treatment. *Nat Nanotechnol.* **2019,** *14* (1), 89-97.

(18) Wang, C.; Wang, X.; Zhang, W.; Ma, D.; Li, F.; Jia, R.; Shi, M.; Wang, Y.; Ma, G.; Wei, W., Shielding ferritin with a biomineralized shell enables efficient modulation of tumor

microenvironment and targeted delivery of diverse therapeutic agents. *Adv Mater.* **2022,** *34* (5), e2107150.

(19) Ge, Y.; Rong, F.; Lu, Y.; Wang, Z.; Liu, J.; Xu, F.; Chen, J.; Li, W.; Wang, Y., Glucose oxidase driven hydrogen sulfide-releasing nanocascade for diabetic infection treatment. *Nano Lett.* **2023,** *23* (14), 6610-6618.

(20) Fu, L. H.; Hu, Y. R.; Qi, C.; He, T.; Jiang, S.; Jiang, C.; He, J.; Qu, J.; Lin, J.; Huang, P., Biodegradable manganese-doped calcium phosphate nanotheranostics for traceable cascade reaction-enhanced anti-tumor therapy. *ACS Nano.* **2019,** *13* (12), 13985-13994.

(21) Zhang, M.; Cheng, J.; Shen, Z.; Lin, P.; Ding, S.; Hu, J., A single-component dual donor enables ultrasound-triggered co-release of carbon monoxide and hydrogen sulfide. *Angew Chem Int Ed.* **2023,** *62* (52), e202314563.

(22) Jin, T.; Lu, H.; Zhou, Q.; Chen, D.; Zeng, Y.; Shi, J.; Zhang, Y.; Wang, X.; Shen, X.; Cai, X., H_2S-releasing versatile montmorillonite nanoformulation trilogically renovates the gut microenvironment for inflammatory bowel disease modulation. *Adv Sci (Weinh).* **2024**, e2308092.

(23) Jia, C.; Guo, Y.; Wu, F. G., Chemodynamic therapy via Fenton and Fenton-like nanomaterials: strategies and recent advances. *Small.* **2022,** *18* (6), e2103868.

(24) Wang, Z.; Ge, Y.; Liu, J.; Shi, P.; Xue, R.; Hao, B.; Wang, Y., Integrating a biomineralized nanocluster for H_2S-sensitized ROS bomb against breast cancer. *Nano Lett.* **2024,** *24* (8), 2661-2670.

(25) Huang, J.; Li, Y.; Zhang, L.; Wang, J.; Xu, Z.; Kang, Y.; Xue, P., A platinum nanourchin-based multi-enzymatic platform to disrupt mitochondrial function assisted by modulating the intracellular H_2O_2 homeostasis. *Biomaterials.* **2022,** *286*, 121572.

(26) He, T.; Qin, X.; Jiang, C.; Jiang, D.; Lei, S.; Lin, J.; Zhu, W. G.; Qu, J.; Huang, P., Tumor pH-responsive metastable-phase manganese sulfide nanotheranostics for traceable hydrogen sulfide gas therapy primed chemodynamic therapy. *Theranostics.* **2020,** *10* (6), 2453-2462.

(27) Wang, J.; Sun, Z.; Wang, S.; Zhao, C.; Xu, J.; Gao, S.; Yang, M.; Sheng, F.; Gao, S.; Hou, Y., Biodegradable ferrous sulfide-based nanocomposites for tumor theranostics through specific intratumoral acidosis-induced metabolic symbiosis disruption. *J Am Chem Soc.* **2022,** *144* (43), 19884-19895.

(28) Zhu, Y.; Archer, W. R.; Morales, K. F.; Schulz, M. D.; Wang, Y.; Matson, J. B., Enzyme-triggered chemodynamic therapy via a Peptide-H_2S donor conjugate with complexed Fe^{2+}. *Angew Chem Int Ed.* **2023,** *62* (22), e202302303.

(29) Wang, G.; Cen, D.; Ren, Z.; Wang, Y.; Cai, X.; Chen, X.; Li, X.; Best, S.; Han, G., Zinc sulfide nanoparticle-decorated fibre mesh to enable localized H_2S-amplified chemotherapy. *Chem Commun (Camb).* **2020,** *56* (31), 4304-4307.

(30) Sen, N., Functional and molecular insights of hydrogen sulfide signaling and protein sulfhydration. *J Mol Biol.* **2017,** *429* (4), 543-561.

(31) Li, J.; Xie, L.; Sang, W.; Li, W.; Wang, G.; Yan, J.; Zhang, Z.; Tian, H.; Fan, Q.; Dai, Y., A metal-phenolic nanosensitizer performs hydrogen sulfide-reprogrammed oxygen metabolism for cancer radiotherapy intensification and immunogenicity. *Angew Chem Int Ed.* **2022,** *61* (18), e202200830.

(32) Ni, X.; Li, X.; Shen, T. L.; Qian, W. J.; Xian, M., A sweet H_2S/H_2O_2 dual release system and specific protein S-persulfidation mediated by thioglucose/glucose oxidase. *J Am Chem Soc.* **2021,** *143* (33), 13325-13332.

(33) Ding, H.; Wei, J. Y.; Fang, L. Y.; Feng, L. L.; Gai, S. L.; He, F.; Wu, L. Z.; Rehman, Z.; Yang, P. P., A multichannel metabolic pathway interference strategy for complete energy depletion-mediated cancer therapy. *Adv Funct Mater.* **2024**, DOI: 10.1002/adfm.202312429.

(34) Ge, Y.; Rong, F.; Li, W.; Wang, Y., On-demand therapeutic delivery of hydrogen sulfide aided by biomolecules. *J Control Release.* **2022,** *352*, 586-599.

(35) Zhang, Y.; Yue, T.; Gu, W.; Liu, A.; Cheng, M.; Zheng, H.; Bao, D.; Li, F.; Piao, J., pH-responsive hierarchical H_2S-releasing nano-disinfectant with deep-penetrating and anti-inflammatory properties for synergistically enhanced eradication of bacterial biofilms and wound infection. *J Nanobiotechnol.* **2022,** *20* (1), 55.

(36) Annalakshmi, M.; Balamurugan, T. S. T.; Kumaravel, S.; Chen, S. M.; He, J. L., Facile hydrothermal synthesis of manganese sulfide nanoelectrocatalyst for high sensitive detection of Bisphenol A in food and eco-samples. *Food Chem.* **2022,** *393*, 133316.

(37) Li, M.; Luo, X.; Lei, S.; Liu, Y.; Guo, H.; Zhang, Y.; Pan, Y.; Chen, K.; Lin, J.; Huang, P., Synchronous interventions of glucose and mitochondrial metabolisms for antitumor bioenergetic therapy. *Adv Mater.* **2023,** *35* (29), e2301099.

(38) Wu, G. L.; Liu, F.; Li, N.; Wang, F.; Yang, S.; Wu, F.; Xiao, H.; Wang, M.; Deng, S.; Kuang, X.; Fu, Q.; Wu, P.; Kang, Q.; Sun, L.; Li, Z.; Lin, N.; Wu, Y.; Tan, S.; Chen, G.; Tan, X.; Yang, Q., Tumor microenvironment-responsive one-for-all molecular-engineered nanoplatform enables NIR-II fluorescence imaging-guided combinational cancer therapy. *Anal Chem.* **2023,** *95* (47), 17372-17383.

(39) Yan, J.; Li, W.; Tian, H.; Li, B.; Yu, X.; Wang, G.; Sang, W.; Dai, Y., Metal-phenolic nanomedicines regulate T-cell antitumor function for sono-metabolic cancer therapy. *ACS Nano.* **2023,** *17* (15), 14667-14677.

(40) Zhang, L.; Zhang, Q.; Hinojosa, D. T.; Jiang, K.; Pham, Q. K.; Xiao, Z.; Colvin, V. L.; Bao, G., Multifunctional magnetic nanoclusters can induce immunogenic cell death and suppress tumor recurrence and metastasis. *ACS Nano.* **2022,** *16* (11), 18538-18554.

(41) Zheng, R. R.; Zhao, L. P.; Huang, C. Y.; Cheng, H.; Yang, N.; Chen, Z. X.; Cai, H.; Zhang, W.; Kong, R. J.; Li, S. Y., Paraptosis inducer to effectively trigger immunogenic cell death for metastatic tumor immunotherapy with IDO inhibition. *ACS Nano.* **2023,** *17* (11), 9972-9986.

(42) Zhao, L. P.; Zheng, R. R.; Kong, R. J.; Huang, C. Y.; Rao, X. N.; Yang, N.; Chen, A. L.; Yu, X. Y.; Cheng, H.; Li, S. Y., Self-delivery ternary bioregulators for photodynamic amplified immunotherapy by tumor microenvironment reprogramming. *ACS Nano.* **2022,** *16* (1), 1182-1197.

(43) Feng, Y.; Qi, S.; Yu, X.; Zhang, X.; Zhu, H.; Yu, G., Supramolecular modulation of tumor microenvironment through pillar[5]arene-based host-guest recognition to synergize cancer immunotherapy. *J Am Chem Soc.* **2023,** *145* (34), 18789-18799.

(44) Gao, F.; Xue, C.; Dong, J.; Lu, X.; Yang, N.; Ou, C.; Mou, X.; Zhang, Y. Z.; Dong, X., Tumor microenvironment-induced drug depository for persistent antitumor chemotherapy and Immune activation. *Small.* **2023**, DOI: 10.1002/smll.202307736.

TABLE OF CONTENTS